

Tomographic profiling of the Jovian rings with images from the Juno spacecraft

A practical investigation of extincted starlight using the Advanced
Stellar Compass

30330 – Image Analysis with Microcomputer
DTU Space

Jakob Konradsen, s113032
Victor Poughon, s131253

Supervisor: John Jørgensen, prof.

18th of December 2014

Abstract

The rings of Jupiter, discovered in 1979 by the Voyager 1 probe, are less understood than other ring systems due to their very faint nature. In 2016 the Juno spacecraft will reach the gas giant and investigate its magnetic and gravitational fields. On board are four units of the Advanced Stellar Compass used for attitude determination. But the primary science orbit will also put those star cameras in positions favourable for a novel investigation of the rings.

When imaging a star through the Jovian rings, light is attenuated by the dust content. Comparing these with the known (non attenuated) irradiance of the same stars, it is possible to obtain measurements of optical depth through the rings at different points. Using tomographic reconstruction techniques yields an image of the internal distribution of the rings dust.

This report exposes a method for reconstructing such an image, through a study of the theory of light attenuation, an analytical investigation of the tomographic problem and experimental work with an engineering model of the star cameras on board Juno.

The main results of this project are the complete mathematical model for profiling the ring, the evaluation of the accuracy of the experimental setup used, and the custom image analysis software intended to validate the most critical steps in the tomographic reconstruction.

Table of contents

Abstract	2
1 Introduction	6
2 Problem formulation	9
2.1 Problem delimitation	10
3 Method	11
3.1 Extinction of starlight	11
3.2 Forward scattering of light from the sun	12
4 Theory	13
4.1 Juno space mission	13
4.2 Structure of the Jovian rings	14
4.3 Light attenuation assumptions in the Jovian rings	16
4.4 Science planning	18
4.5 Star recognition	19
4.6 Starlight intensity in the camera	20
4.7 Tomography	20
5 Analysis	23
5.1 Image acquisition and smearing	24
5.2 Star recognition and identification	24
5.3 Intensity and optical depth estimation	26

5.4	3D ray reconstruction	27
5.5	Planar reduction	28
5.6	Tomographic image reconstruction	29
6	Model and Validation	32
6.1	Experimental setup	32
6.2	Radiometric calibration	33
6.3	Star rendering	39
6.4	Planetarium using the Hipparcos catalog	40
6.5	Optical depth	41
6.6	Juno orbit simulation with SPICE	45
6.7	Software	45
7	Conclusion	46
8	Future work	47

List of symbols

Symbol	Description
τ	Optical depth
τ_i	Optical depth measurement
τ_{min}	Minimum optical depth measurable
$f(x, y)$	Optical density distribution
δA	Integration area
δt	Shutter time
$b(\lambda)$	Irradiance
$q(\lambda)$	Quantum efficiency
N	Number of elections
ΔN	Minimum measurable difference of electrons
$p(i, j)$	Pixel value in (i,j)
I	Intensity
I_0	Non-attenuated intensity
I_{ref}	Intensity of reference star
m	Stellar magnitude
m_{ref}	Stellar magnitude of reference star
$G_{\alpha, \sigma}(x, y)$	Gaussian function
α	Gaussian function amplitude
σ	Gaussian function spread
RA	Right Ascension
DE	Declination
N	Number of sample points
M	Number of measurements
\mathbf{G}	Model matrix (size $M \times N$)
L_i	Integration path of measurement i
f_j	Values of image sample points
$h_j(x, y)$	Interpolation kernel function
$g(x, y)$	Interpolation kernel function
(ρ, φ, z)	Cylindrical coordinates

1 Introduction

In 2016 the Juno spacecraft will enter orbit around Jupiter. Its main mission is the study the gravitational and magnetic fields of the planet, but several other scientific goals are being planned. It will enter a highly elliptical orbit with a perigee as low as 4500 km. It will allow the spacecraft to fly below Jupiter's harmful radiation belt, thereby allowing for less shielding of science equipment. Juno carries four units of the Advanced Stellar Compass instrument, used mainly for attitude determination. Other than acquiring the attitude of the spacecraft, the position of the star cameras and the planned science orbits allow a unique observation scan of Jupiter rings, also known as the Jovian rings.



Figure 1 – Artist view of Juno at Jupiter.

Jupiter's very faint rings were first discovered in 1979 by the Voyager 1 mission [12], but later further investigated by other space missions and Earth-based observations, although their structure, size, thickness and composition are poorly known to this day. The difficulty lies in their very faint nature, making Earth based observations almost impractical. The composition and density of the Jovian rings is of great interest to astronomers as the specific characteristics can reveal information about the age of Jupiter, and also the origin of the dust.

The Advanced Stellar Compass (figure 2) is a 20 mm focal length visible light camera. It is very accurate for attitude determination and provides arcseconds precision.

By using the star cameras mounted on Juno, and utilizing the science orbits already in place, an inspection of the Jovian rings can be used for making a tomographic profile of the Jovian rings, as shown in figure 3. This report deals with answering if this is possible using a method called occultation profiling. And if it is in fact possible



Figure 2 – Star camera engineering model used for the experimental part.

using this method, what are the restrictions in terms of resolution feasibility and how can the tomographic mapping be implemented when the image data is acquired.

Furthermore, a experimental setup is tested for its resemblance to the real scenario. The obtained sensitivity in the laboratory is measured and characterized.

By studying the existing litterature, assumptions about the Jovian ring system are acquired and form the basis of an analysis on how a tomographic mapping of the Jovian rings can be implemented. As mentioned, an occultation profile method is suggested which utilizes the extinction of starlight through the rings, which is closely related to the density characteristics of the rings through which the starlight passes. By utilizing a discrete version of the continuous tomographic problem, together with a planar projection of the ring system, a method is suggested which could be used for mapping the radial density variations of the Jovian rings.

Then, considerations of the needed sensitivity of the measurement system are taken into account, forming a basis of analysis for the required exposure times needed to gain the sufficient sensitivity to be able to measure the very faint rings. After theoretical observations, a setup consisting of an engineering version of the star cameras used onboard Juno and a video projected "star plane" is described. It is used with the purpose of determining the sensitivity and precision of both the setup and the camera, and to demonstrate critical parts of the proposed method.

The findings of this has determined that the sensitivity which was possible to obtain in the laboratory does not suffice for what is estimated to be in the Jovian rings. Major noise sources specific to the experimental setup are found and described.

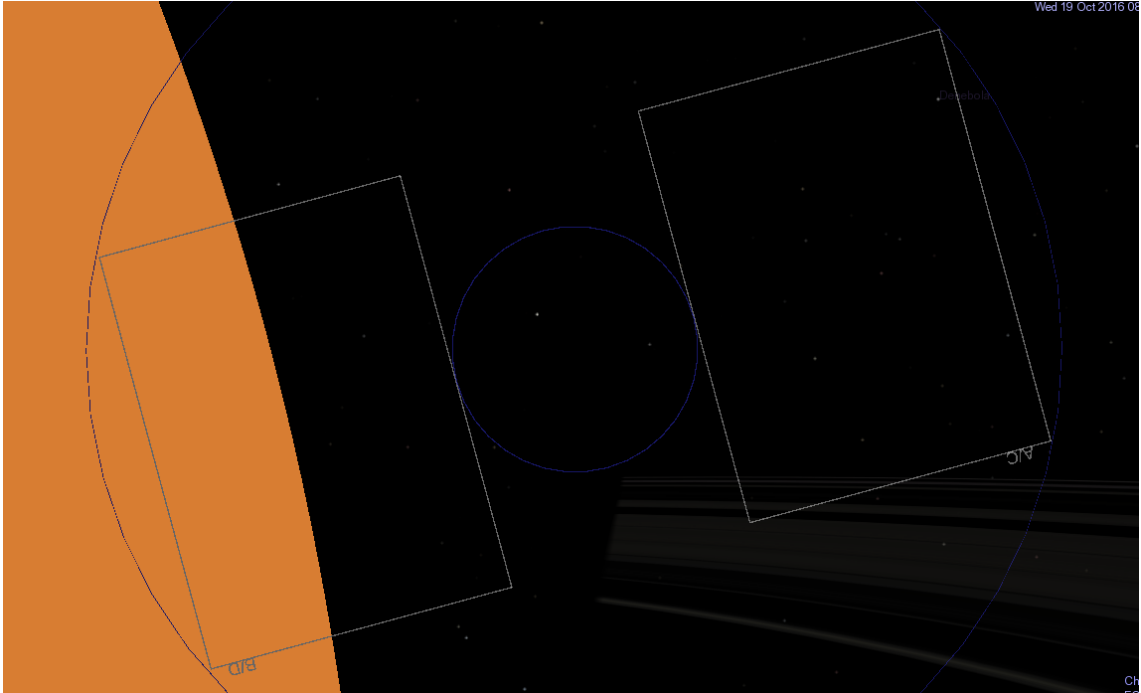


Figure 3 – Field of view of the star cameras as Juno passes within Jupiter rings on October 19th 2016. Part of the ring is in Jupiter’s shadow.

This report describes the major considerations necessary for implementing a tomographic mapping of the Jovian rings using the ‘occultation profiling’ method. The theoretical background for determining the internal structure of the rings is described, with emphasis on acquiring the ray data from images. Furthermore, basic extinction theory is described, and current data on the optical depths of the Jovian rings is presented. The theory is applied in an analysis where a method is exposed in details. Finally, the practical laboratory setup is exposed. The attained sensitivity is measured, and results illustrate relevant parts of the analysis.

2 Problem formulation

When the Juno space mission [9] will orbit Jupiter at aprox. June 2016, it will be able to take images using the Advanced Stellar Compass and send these back to Earth via the Deep Space Network, although at a very high cost, both econommically and powerwise. The topology of the rings of Jupiter, also known as the Jovian rings is not known to a great extend. Therefore it is interesting to use the Juno spacecraft, and the star cameras mounted on this to map the Jovian rings. By using the two sets of star cameras mounted on Juno, it is possible to obtain sets of images of stars through and besides the Jovian rings and their light intensities, to be used for a tomographic mapping of the Jovian rings. Although due to the fact that the images can not be obtained at an infinite amount, the particle size and light scattering characteristics of the dust making up the Jovian rings is not exactly known and that a method for determining the tomographic map of the Jovian rings has not yet been developed, this poses a series of questions:

- What are possible methods for determening the structure of the Jovian rings, and which one could be developed during this project?
- A method to be used for determining a profile of the Jovian rings, is to use the extinction of starlight through the occulated areas of the Jovian rings. How could a method be developed that uses the extinction of starlight through the Jovian rings in the occulated area?
- What kind of data is needed in order to perform a probable tomographic mapping of the Jovian rings, and what will be the outcome data?
- How can a mathematical model be found for determining the topological map of the Jovian rings in regards of the position, attitude and attenuation information?
- If a method is proposed for mapping the rings, how can this method be validated, and what are the critical parts of a laboratory test-setup which can validate the suggested method?

2.1 Problem delimitation

This project focuses on the tomographic mapping of the jovian rings, with information estimated to come from the Juno mission. The images estimated to come from the Juno spacecraft are rotational and linear smeared, but this project will assume already de-smeared images, and will therefore not focus on the de-smearing, both linear and rotational of the images.

Also the work in this project will assume that the location and attitude of the spacecraft is known, and will therefore not focus on getting the attitude and location from star camera information.

This project will focus on the method of extinction of starlight through the Jovian rings, and therefore not on another method of forward scattered light from the sun.

Last, this project will focus on making a tomographic map of directly visible extinction of starlight, and will therefore not focus on taking into account the scattering physical characteristics of the dust estimated to make up the Jovian rings.

3 Method

In this chapter two different methods for profiling the Jovian rings are proposed, and one is chosen for further investigation and testing.

3.1 Extinction of starlight

This method is based on the fact that the intensity of starlight is reduced when it passes through clouds of dust, also called extinction [8]. This method proposes to utilize images taken by the star cameras onboard Juno of stars before and after getting "behind" the Jovian rings. By comparing the apparent brightness of stars from without extinction from Jovian rings, and those influenced by extinction, and the attitude and position of the spacecraft, and therefore also the angle to the rings, information about the extinction at different angles can lead to a tomographic mapping of the rings.

As the extinction of starlight is dependent on both the density and physical characteristics of the dust, physical characteristics of the dust could also be found, although this is not the aim for this project. The amount of extinction is described in [8] as being a product of:

$$\tau_a = \text{const} \cdot f(\lambda) \quad (1)$$

Where the constant describes the extinction of light along the line of sight, and $f(\lambda)$ being the extinction curve related to the physical characteristics of the dust in sight. This means that the extinction of light is dependent of the density of dust.

By using images in the occultated area of the Jovian rings, light from the Sun can be omitted, and therefore it is assumed that light observed comes purely from the stars viewed. It should however be considered how reflected light from the spacecraft itself influences images taken of the rings at a close range.

This method is also described in [2] as 'occultation profiles', under which two different categories are described, one of which is the method described above. As stated "Occultation experiments are capable of obtaining much finer spatial resolution than images, although only along a one-dimensional track" [2] which is of great use for this project. There is however also an other disadvantage as it is stated that experiments with a sensitivity of $\tau \lesssim 10^{-3}$ has never been obtained, and that detecting dusty rings with this method has not yet been done.

3.2 Forward scattering of light from the sun

The second method considered, is to use the light from the Sun that is forward scattered by the Jovian rings. This method uses the fact that the forward scattered light from the Sun can be seen from the occultated area of Jupiter where the direct light from the Sun is not visible, and therefore not introducing noise into the image.

This method is also described in [11], which uses the fact that dust highly forward-scatters light, and that the phase and intensity of this light is connected to the density of the dust (among other characteristics). From this information a mapping of the rings can be made. It is also using this method that the extend of the Jovian rings are mainly determined today.

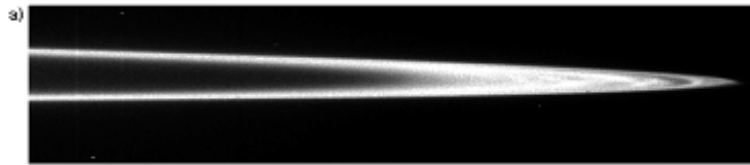


Figure 4 – Forward scattered light from Jupiters rings as seen from the Galileo experiment. Here seen as a mosaic of different images. From [11]

4 Theory

4.1 Juno space mission

The Juno mission is a part of NASA's New Frontiers mission and was launched on August 5th 2011. The purpose of the Juno mission is to gain insight into the origin and evolution of Jupiter [10]. The spacecraft is a spinning spacecraft due to less complexities in science payload data-acquisition and to avoid more complex instrument scan platforms. The spacecraft spins with about 2 rpm during science operations, which in hand affects the acquiring of images, both for star tracking and thereby attitude determination [10] and also, of course, for this project. The spacecraft is depicted in figure 5 below:

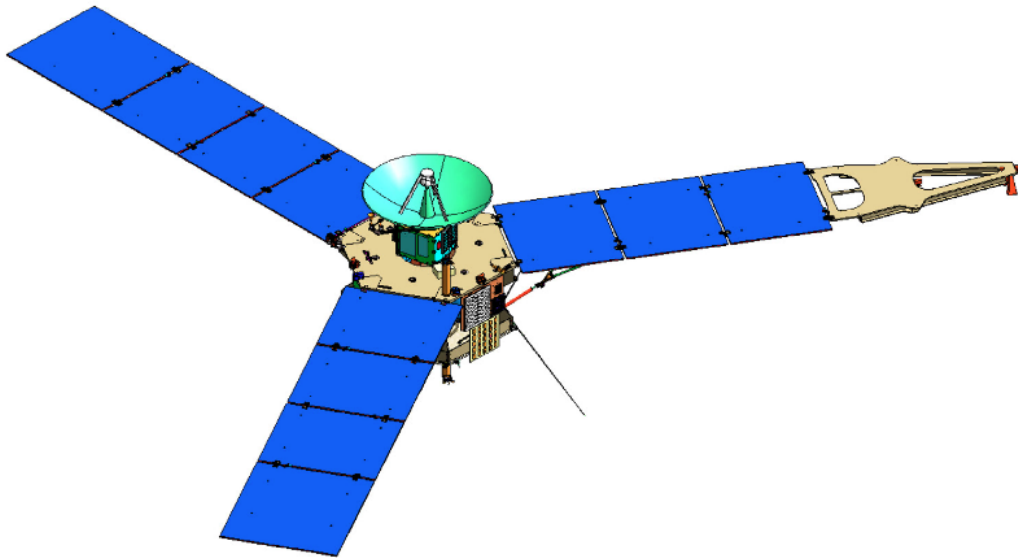


Figure 5 – Overall view of the Juno spacecraft. From [10]

The Juno space mission aims at covering Jupiter through several orbits, although it is not yet determined how many. The planned science orbits are depicted in figure 6.

As seen the orbits covers Jupiter in a web, thereby widely covering the planet's surface. What is not seen on this picture is of course the Jovian rings which are of interest for this project. These lay almost in the equatorial plane, and can at the right times be observed by the star cameras on Juno.

The Juno spacecraft uses two sets of star trackers for determining the attitude of the spacecraft during flight. These can also be used for acquiring images and sending

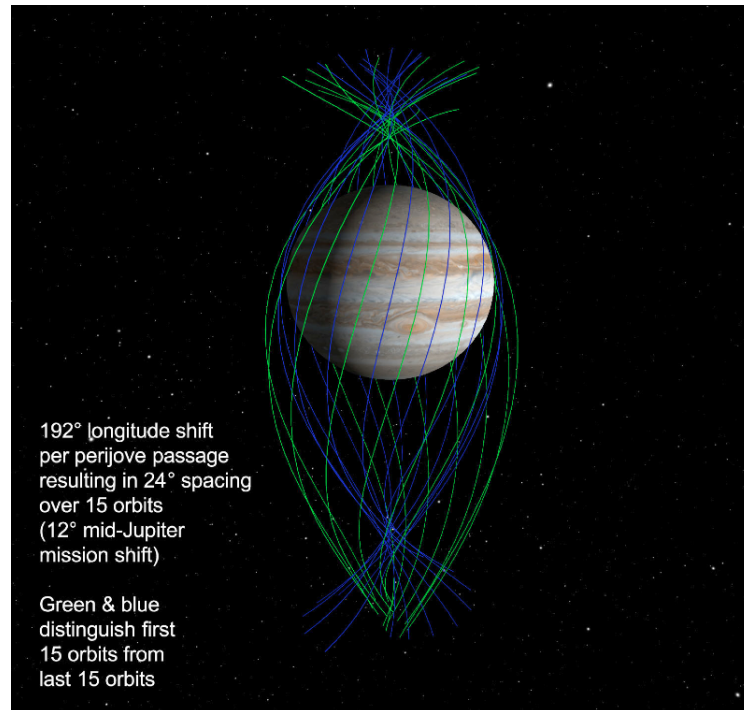


Figure 6 – The web covering Jupiter during flybys. From [10]

these back to Earth for analysis. The cameras point away from the rotation axis at a 13° angle away from each other. Together with the spinning nature of Juno, this makes for images which can be taken through the ring in the occultated areas of the ring. An example of such is shown in the introduction (figure 3).

4.2 Structure of the Jovian rings

The Jovian ring system was first discovered in 1979 by images taken from Voyager 1. It is thereby the first dusty rings to be observed from space. It has later been observed in greater detail from Voyager 2 and Galileo [2]. The ring system has three main components: the Halo, the Main Ring and the Gossamer Rings, which can also be seen on figure 7. The outer rings are strongly visible in forward scattered light as it can be seen on this image from the Galileo mission (figure 8).

The rings are very faint compared to rings of Saturn or Neptune, which is also the reason why they were discovered as late as they were. Jupiter has rings with optical depths of 10^{-6} whereas Saturn has rings with optical depths up to 0.03 [2]. This has made them impossible to observe in great detail from Earth, which is also why it is of great interest to observe with the Juno mission.

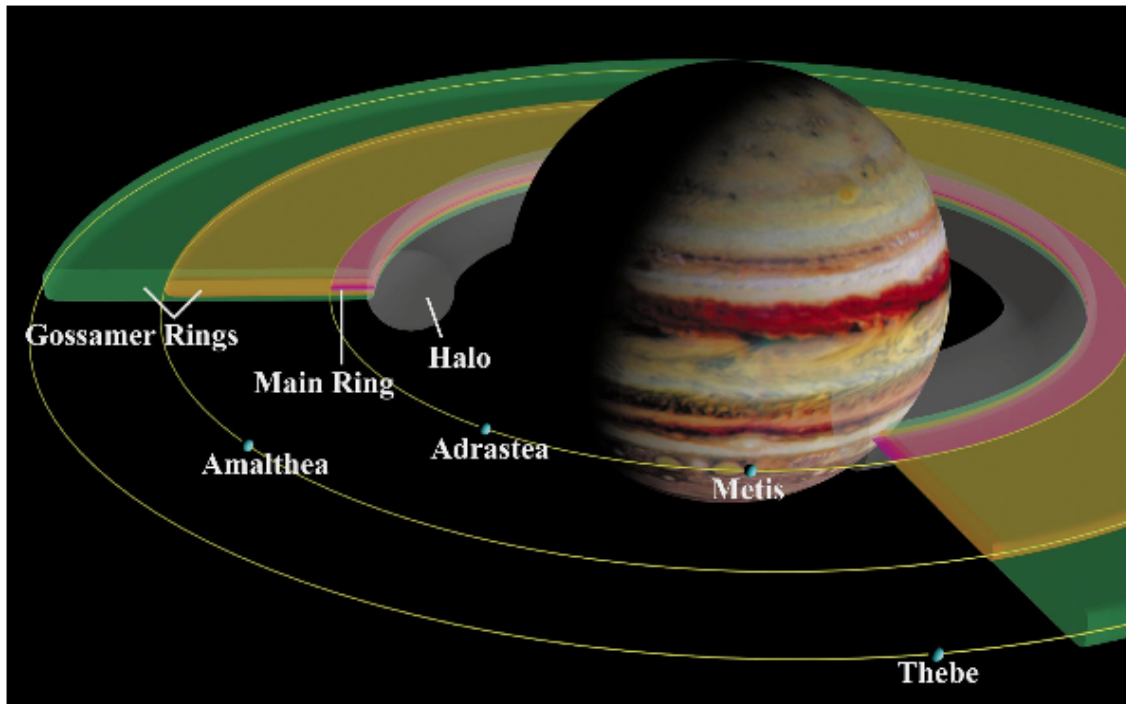


Figure 7 – The composition of the Jovian rings. From [11]

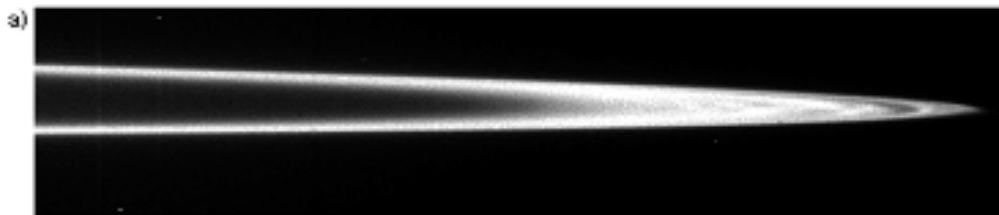


Figure 8 – Forward scattered light from Galileo. From [2]

JUPITER					
Halo	92 000– 122 500	10^{-6}	100	?	12 500 km thick
Main Ring	122 000– 128 980	$3 \cdot 10^{-6}$	$\sim 50?$	$q = 2.5 \pm 0.5$	Brightness dip near Metis' orbit; bounded by Adrastea
Amalthea Gossamer	$\leq 129\,000$ – 182 000	10^{-7}	100?	?	2 600 km thick; bounded by Amalthea
Thebe Gossamer	$\leq 129\,000$ – 226 000	$3 \cdot 10^{-8}$	100?	?	4400 km thick; bounded by Thebe

Figure 9 – The Jovian rings extend from Jupiter. From [11]

The rings lay almost in the equatorial plane. They extend from Jupiter as described by figure 9. As it can be seen, the rings (besides the halo) are very thin compared to the radial length. The extend of the rings are not completely defined, as the images which the data is based on, are not total definitive. There is some diversion in where exactly the different rings starts and stops from image to image [11], which is the cause of the uncertainty.

4.3 Light attenuation assumptions in the Jovian rings

Current knowledge about the Jovian rings comes mostly from image data from Earth-based telescopes and the satellite missions that have orbited Jupiter [17]. This section will expose and justify assumptions regarding the behavior of light through Jupiter rings.

4.3.1 Optical density

Beer-Lamberts law

Beer-Lamberts law [14] states that the relation between incident light intensity into a medium I_0 , and the intensity of light leaving the medium I obeys:

$$\frac{I}{I_0} = e^{-\sigma l N} \quad (2)$$

Where σ is the attenuation cross section, N is the density of attenuators and l the geometric length of the path through the medium. This implies that if the path length of the light ray and the cross sectional area of the light beam is known, the density information can be obtained from this equation.

It should be noted that this relation is different for different wavelengths, and thus is wavelength dependent. This links closely to the transmittance described below.

Transmittance

The transmittance describes how well a medium lets light pass through it, and is defined as:

$$T_\lambda = \frac{I}{I_0} \quad (3)$$

As seen, the transmittance relation gives a non-linear relation between incident light intensity and observed light intensity, which is unwanted. This can be omitted if the absorbance is used instead.

Absorbance

The optical density, also denoted as absorbance (A), describes the logarithmic relation between incident light intensity upon a medium and the light intensity of light leaving the medium, and therefore gives a linear relation with the absorbent density:

$$A_\lambda = \ln\left(\frac{I_0}{I}\right) = \ln(T_\lambda) = -\sigma l N \quad (4)$$

It is seen that this relation is linear, and therefore preferred instead of the transmittance.

Optical depth

As most literature on the Jovian rings deals with optical depth, the relation to transmittance and absorbance is described. Optical depth τ is defined as:

$$\frac{I}{I_0} = e^{-\tau} \Rightarrow \tau = -\ln\left(\frac{I}{I_0}\right) = -\ln(T_\lambda) \quad (5)$$

Further more if the relation to absorbance is wanted:

$$A = 2 - \log(\tau) \quad (6)$$

4.3.2 Estimations of absorbance of Jovian rings

The absorbance of the rings are estimated based on current literature based on the recent space missions to Jupiter. There is not a concurrent value of the size of the optical depth of the different ring parts as different articles state different values. Nevertheless, an order of magnitude is given, and forms the basis of evaluation for what to expect. The absorbance is estimated in the visible light spectrum, as the star cameras can observe light in this area of wavelengths.

	Location (width)	Optical depth	Dust fraction (%)	Power-law index	Notes
<i>Jupiter</i>					
Halo	92 000–122 500	10^{-6}	100	?	12 500 km thick
Main ring	122 000–128 980	3×10^{-6}	~ 50 (?)	$q \leq 2.5$	Bounded by Adrastea
Almalthea	129 000–182 000	10^{-7}	100 (?)	?	2000 km thick
Gossamer					
Thebe	129 000–226 000	3×10^{-8}	100 (?)	?	4400 km thick
Gossamer					

Figure 10 – Estimated optical depths of Jovian rings from [4]

The absorbance is calculated using equation (6), to be the following for the different ring parts, using numbers from the above table.

Ring	absorbance
Halo	15,81
Main ring	14,71
Almalthea Gossamer	18,11
Thebe Gossamer	19,32

This gives a good indication of what absorbances to expect through the Jovian rings.

Furthermore, as none of the articles found describe at what angles the optical depths are taken, it is assumed these numbers holds true for most angles, except at very steep angles close to the ring plane. This is due to the fact that the vertical extend of the rings are very small compared to the width of the rings, as described in section 10.

The absorbances mentioned are estimated to be in the visible light spectrum or at least to an extend with the same absorbance as in the visible spectrum.

4.4 Science planning

As mentioned before there are several limitations to acquiring images from star cameras on the Juno spacecraft. These are due to economy, power and image acquisition time due to shutters on the star camera and download times. As of this, planning when to acquire images and how many is needed becomes important. Further more it is needed to know what kind of topological resolution is needed, as this has an impact on where and how many images are acquired.

The wanted resolution of the tomographic measurements is not something that can be fully determined. An ideal situation would be to have infinite resolution at infinite many points, but as this is not possible a trade-off has to be made.

As one of the goals of the topological mapping is to know the extend of the different rings, one might look at figures 10 and 9. It can be seen that there is not a definitive conclusion to the extend, as the different data shows slight deviations in vertical extend.

In order to determine the vertical extend, a vertical resolution of 200 km should suffice, mainly for the main ring and the gossamer rings. This is in the area of 1/10th of the smallest vertical extend. In terms of radial resolution, the extend is better known, and therefore the same resolution should suffice.

The other goal is to determine local densities. As the rings are large in extend, at least compared to the individual sub-rings and the planet itself, the radial resolution does not have to be very fine. A resolution of 500 km should suffice, which is 1/12th the extend of the main ring.

If compared to images taken of Saturn, Neptune and Uranus with the cameras on the Voyager mission, a resolution of 10-100 km were acquired [2] also with a occultation experiment. Therefore the wanted resolution should be possible to acquire.

4.5 Star recognition

The tomographic analysis of the Jovian rings relies on getting data from star intensities at different places on the rings. This acquisition is to be done from the same stars, but at different times of orbit. Therefore it is needed to recognize which stars are being measured. For this purpose the Hipparcos star catalogue can be used.

The Hipparcos star catalogue is a collection of 118,218 stars mapped with a high precision by the Hipparcos mission in 1989 to 1993. This catalogue holds the position, parallaxes and proper motion of all the stars in the catalogue [13].

The information from the Hipparcos catalogue, together with attitude information from the Juno mission at image sampling times, can be used for determining which stars are being monitored, and thereby logging the intensities of the same stars to be used for the tomographic profiling.

As the test setup used in section 6 is not a perfect scenario, where a series of factors will influence the precision of position, an algorithm for detecting the stars from the position from the catalogue $p_c(RA_c, DE_c)$ is considered:

$$p_{star} = p(RA_c \pm RA_{err}, DE_c \pm DE_{err}) \quad (7)$$

If an observed star is within this range of right ascension and declination it is considered to be the same star. Of course this error will be larger for the test setup used in this report than in a real scenario.

4.6 Starlight intensity in the camera

In order to determine how much starlight from a specific star is attenuated the actual starlight intensity can be calculated given the relation:

$$N = \delta A \delta t \int b(\lambda) q(\lambda) \delta \lambda \quad (8)$$

where δA describes the area of integration in the image sensor, δt the integration or shutter time, $b(\lambda)$ the incident light and $q(\lambda)$ the quantum efficiency [6]. This relation yields a result for how many electrons are observed by the sensor N and is related to pixel value which is used as a measure for light intensity.

4.7 Tomography

Tomography is the process of reconstruction the internal structure of a system from indirect measurements. It concerns itself broadly with electromagnetic radiation, sounds waves, laser pulses or even seismic waves. The observation is *indirect* because the system senses the effects of a physical process which is dependent on the physical parameters of interest. The reconstruction problem is then solved by inverting the model known from the physics of the imaging system.

Tomographic imaging systems use a very wide range of phenomena, for example: light from many parts of the electromagnetic spectrum, electron-positron annihilation, muons, ions or magnetic particles. Because of this and the indirect nature of the problem, the focus in tomography is usually on the data processing methods and the different ways of solving the same task [5].

The medical imaging field is an important user of tomography. It has driven the development of the technology for the great benefit of imaging the interior of the body without direct access. In general, for any problem where indirect measurements are available as the result of a well known physical process, tomography enables the reconstruction of the internal distribution of those physical parameters. In that sense, deducing the internal structure of the Jovian rings from indirect measurements of starlight passing through them is a tomographic problem.

Unlike medical imaging, where the radiation patterns, intensities and exposure times are fully controlled, mapping the Jovian rings with the Juno spacecraft is heavily constrained by the existing primary mission objectives and parameters. Optical wavelength is atypical for tomography, but is used in the context of the star camera.

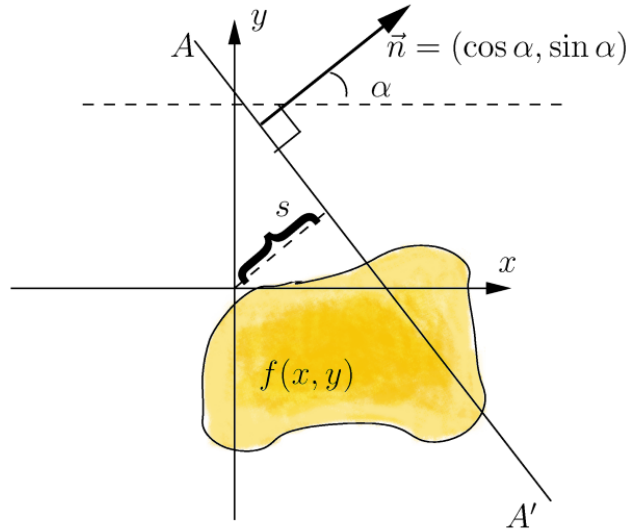


Figure 11 – Tomographic reconstruction of a continuous medium with the Radon transform. Image from Wikipedia [15].

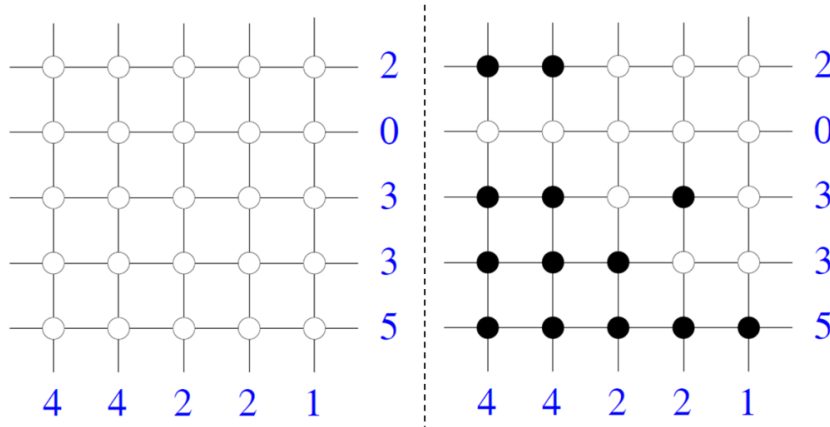


Figure 12 – Example of a discrete tomographic reconstruction problem and its (non unique) solution. Image from Wikipedia [3].

Finally, the image to be reconstructed is the optical depth distribution of the Jovian rings which is very faint. It is expected to be around 10^{-6} (figure 10) which is many orders of magnitudes below what is normally used in medical imaging. Nevertheless, the mathematics are the same and it is expected that the chosen instrument will provide an exciting new application of tomography.

Different approaches exist for solving inverse reconstruction problems. They are divided into two primary groups: analytical and discrete methods, as illustrated by figures 11 and 12. Analytical methods assume a smooth, continuous medium and are typically based on variants of the Radon transform (or X-Ray transform):

$$Rf(\alpha, s) = \int_{M \in A(\alpha, s)} f(M) dM$$

where $f(M)$ is the continuous function describing the image, and α, s define the integration line A . Inversion of the Radon transform is well developed and based on *inversion by backprojection*. The analytical method is powerful, but limited to cases where the assumption of continuous and complete observations exists. In 2D for example, this requires coverage of all observation angles. In that case, the inversion is straightforward and robust.

However more constrained problems require the use of discrete methods, which are more flexible in modeling, problem geometry and inversion methods. In this setting, the image is represented by discrete pixels, or voxels in 3D, and the forward model is any general function that explains the observations as a function of the image values. Section 5.6 will show how the problem formulated here can be stated as a linear inverse problem:

$$\mathbf{d} = \mathbf{G}\mathbf{f}$$

where \mathbf{d} is the vector of observed data, \mathbf{G} is a model matrix, and \mathbf{f} is the image of the ring to be reconstructed.

5 Analysis

This section consists of the detailed analysis of the stated problem. A method is proposed for processing Juno star camera images and inferring the optical depth distribution of the interior of the Jovian rings. Building upon the previous theory section, the method consists of six processing steps:

Image aquisition

The images are acquired by the spacecraft, downlinked to Earth and pre-processed to correct smearing. Attitude and position data is also collected.

Data: Image data from a star tracker.

Processing: Downlink

Star recognition and identification

Visible stars in the image are extracted and identified. This step carefully eliminates noise sources and potential non stellar objects (Jupiter and its moons).

Data: Visible stars, their intensities and image coordinates.

Processing: Threshold, connected components, classification.

Intensity and optical depth estimation

Optical depth is estimated by comparing two observation of the same star: one at reference intensity and others with attenuation caused by the ring.

Data: Optical depths observations at specific positions and attitudes.

Processing: From pixel intensity to optical depth (equation 5).

3D ray reconstruction

Knowing the observations positions and attitude the 3D line through the ring and to the star is reconstructed in Jupiter centered coordinates.

Data: Image rays in Jupiter centered coordinates.

Processing: Conversion of angles and pixel coordinates to a 3D vector.

Planar reduction

The problem is reduced from 3D to 2D by projection in cylindrical coordinates.

Data: 2D path integrals through a virtual planar ring section.

Processing: Projection in cylindrical coordinates.

Tomographic image reconstruction

Finally, the inverse problem is solved to produce an internal image of the ring. The image is in a vertical half-plane parallel to Jupiter's rotation axis.

Data: Radial profile of the ring.

Processing: Discrete inverse problem.

5.1 Image acquisition and smearing

As mentioned in section 4.1 the Juno spacecraft is spinning at about 2 rpm during science operations. This poses a series of considerations to the question of tomographic mapping from the image data.

As the optical depth of the rings are very small (approx. $\tau = 10^{-6}$) the shutter time for the star cameras has to be very high to gain a better sensitivity. This means that the images will be subject to motion-smear. This will be a superposition of both the rotation of the spacecraft and the linear motion of the spacecraft's flight through space. This smear can to some extent be removed by de-smearing the images (although not covered in this report), although this might not be of benefit to the analysis of the image data.

The purpose of de-smearing the images is mainly to get a better visual output of the images. This is not needed as the integral of the light intensities of the stars are the same after a de-smearing algorithm if the filter is a neutral filter. An other point would be to be able to use the same algorithms used in "still" images, where light intensities and other features are found from images without motion-smear. None of the above will be dealt with further in this report.

The motion smear together with the observed motion of the spacecraft can be used as a scanning method and thereby observing an area of the rings. As the image data is an integral of the scanned area, the scanned optical depths are considered homogeneous along the scanned line in the rings. This of course implies that the scanned length is shorter than the wanted resolution, or puts a limit to the shutter time if a certain resolution is wanted.

5.2 Star recognition and identification

5.2.1 Identification of stars from background

Before the intensity measurements can be done, it has to be determined what is the background and what is stars. This is to be done via a thresholding of the sample image with a certain threshold value t :

$$p_{i,j} = \begin{cases} p_{i,j} & \text{if } p_{i,j} > t \\ 0 & \text{if } p_{i,j} \leq t \end{cases} \quad (9)$$

Where the threshold value t is determined by histogram analysis of the image, to determine the noise level.



Figure 13 – Motionsmear in stars, image from Juno spacecraft.

5.2.2 Connected components

In order to determine where the stars are and how big they are, a modified connected components algorithm is used. The algorithm first of all scans an image from the top-left corner, and if it finds an area where a value is above 0 (after above mentioned thresholding) it starts extracting a rectangular region-of-interest (ROI) around the detected star. From here the algorithm checks if a value is observed on any of the four sides, if so, that side is expanded to also cover this pixel. It does so until none of the sides have connected pixels with a value above 0. When this has been done the area is extracted and saved, and the ROI is removed from the image in order not to be counted in again. A depiction of how the algorithm works is made below:

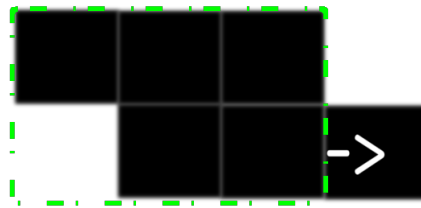


Figure 14 – The ROI of the modified connected components algorithm expands at sides where values of above zero are found.

This algorithm is chosen on the basis that it is expected to have a great separation between identified stars, and that overlapping therefore is not present. Also the wanted output of the algorithm was to extract images of each of the stars, which is why a rectangular extraction is used.

5.3 Intensity and optical depth estimation

As described in section 4.6, the intensity obtained from the camera is defined by:

$$N = \delta A \delta t \int_0^\infty b(\lambda) q(\lambda) d\lambda$$

In the obtained images, a star is not only confined to a single pixel. Therefore a sum of the entire are has to be made, defined by:

$$p_{tot} = \sum_{i,j} p_{i,j} \quad (10)$$

Where p_{tot} is the total pixel value, and $p_{i,j}$ describes all pixels within a certain star. This sum will then directly relate to the intensity of a single star.

5.3.1 Weighted center of mass

In order to determine the center of star, a weighted center of mass algorithm is used. This will output a center of the observed stars based on weighted average in both x and y direction of the star, in a continuous format of pixels.

$$\begin{aligned} M_{10} &= \sum_{i,j} p(i,j) i \\ M_{01} &= \sum_{i,j} p(i,j) j \\ M_{00} &= \sum_{i,j} p(i,j) \end{aligned} \quad (11)$$

$$\begin{aligned} \bar{x} &= \frac{M_{10}}{M_{00}} \\ \bar{y} &= \frac{M_{01}}{M_{00}} \end{aligned}$$

The center of mass (\bar{x}, \bar{y}) is weighted by the intensity at the different pixels.

5.3.2 Optical depth estimation

As defined in section 4.3, optical depth τ is the logarithmic ratio of the non attenuated intensity I_0 to the measured intensity I :

$$\tau = \ln \frac{I_0}{I}$$

But what is the minimum optical depth that can be detected? This minimum value τ_{min} depends on intensity, sensitivity of the detector and exposure time. Ignoring wavelength dependence, equation (8) becomes:

$$N = \delta A \delta t I q$$

where q is the quantum efficiency of the detector. However the signal N is discretized and sampled to fit in, usually, a byte. This limits the achievable dynamic range of magnitudes, and also sets the minimum difference of electrons measurable, ΔN . It is determined by the sampling resolution of N and the expected noise level.

Optical depth is measurable when:

$$\delta A \delta t q (I_0 - I) > \Delta N$$

Therefore τ_{min} is such that:

$$\begin{aligned} \delta A \delta t q (I_0 - I_0 \exp(-\tau_{min})) &> \Delta N \\ \tau_{min} &> \ln \frac{1}{1 - \frac{\Delta N}{\delta A \delta t q I_0}} \end{aligned} \quad (12)$$

This relation illustrates the expected dependence of τ_{min} on the initial intensity of the observed star, the sensor area, the shutter time and the detector sensitivity. It also shows the parameters that can be changed to obtain a better sensitivity to optical depth. Increasing the shutter time is the most interesting possibility, because in space, observation conditions are fairly stable and allow large integration times.

5.4 3D ray reconstruction

Let the camera position be (X, Y, Z) in Jupiter-centered coordinates. The direction of the observed star is assumed known. Stars' directions are usually represented in the Equatorial coordinate system by right ascension RA and declination DE. A unit vector \mathbf{a} in the direction to the star is:

$$\begin{cases} a_x = \cos(\text{DE}) \cos(\text{RA}) \\ a_y = \cos(\text{DE}) \sin(\text{RA}) \\ a_z = \sin(\text{DE}) \end{cases}$$

The parametric equation of the line (or *ray*) from the camera to the observed star is:

$$\begin{bmatrix} X + \mu a_x \\ Y + \mu a_y \\ Z + \mu a_z \end{bmatrix}, \forall \mu \in \mathbb{R}^+ \quad (13)$$

So the data at this point are intensities, and rays characterised by a point and vector in space.

5.5 Planar reduction

In this section an assumption is proposed: the ring is symmetric around Jupiter's rotation axis. Following this assumption, the problem can be reduced to a vertical cross section of the ring.

The mathematical reason for carrying this transformation is the great advantage of reducing the problem from three to two dimensions. It is extremely useful when trying to reconstruct the internal structure of the ring for different reasons.

First, the density of observations is much greater. A two dimensional representation of the ring allows a much greater ratio of data to model parameters. In turn, the reconstructed result will be more robust and certain. Additionally, the tomographic reconstruction will be easier to implement and also visualize. Finally, when representing the ring in computer memory, a 2D ring allows a much simpler data structure. Only sample points on a regular grid are needed. It is possible to simply use a matrix together with a resolution parameter, and use an image format for storage on disk or visualization.

All points at the same radial distance from Jupiter's Z axis are equivalent. A point (x, y, z) in Jupiter-centered coordinates is projected by rotation around the Z axis on the vertical (X, Z) half-plane. This is accomplished by converting to cylindrical coordinates and setting $\varphi = 0$.

$$\begin{cases} \rho = \sqrt{x^2 + y^2} \\ \varphi = 0 \\ z = z \end{cases} \quad (14)$$

Figure 15 shows how, in the new plane in which the problem is considered, this point is represented by $(x_p, y_p) = (\rho, z)$.

However, in the projected half-plane the measurements rays are not straight lines. The projection of a ray is obtained by combining equations (13) and (14):

$$\begin{aligned} & \begin{cases} \rho = \sqrt{(X + \mu a_x)^2 + (Y + \mu a_y)^2} \\ \varphi = 0 \\ z = Z + \mu a_z \end{cases} \\ \Leftrightarrow & \begin{cases} x_p = \sqrt{(X + \mu a_x)^2 + (Y + \mu a_y)^2} \\ y_p = Z + \mu a_z \end{cases} \\ \Leftrightarrow & x_p^2 = \left(X + \frac{y_p - Z}{a_z} a_x \right)^2 + \left(Y + \frac{y_p - Z}{a_z} a_y \right)^2 \end{aligned}$$

which is the equation of a conic section. Figure 16 gives an example of this ray and its position in Juno's orbit. The next section will show how the coefficients of the

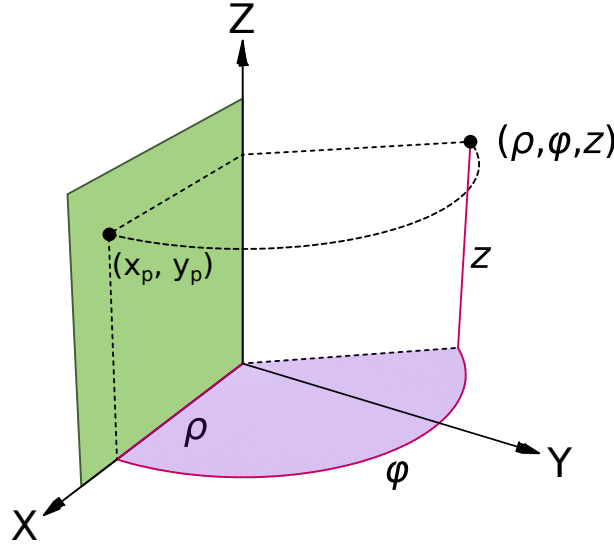


Figure 15 – Projection to the $\varphi = 0$ half-plane in cylindrical coordinates geometry.

forward model are computed numerically to account for the uncommon situation of curved measurement rays. Using a discrete method for tomography is flexible and allows an arbitrary observation geometry, as long as it is numerically defined.

5.6 Tomographic image reconstruction

The method for tomographic reconstruction chosen here is discrete. The result of line integrals are observed through the medium and it is desired to reconstruct the internal structure. One measurement τ_i , $i \in [1, M]$ of a star intensity is the result of a path integral along the path L_i from the camera to the star. This path is known to be a conical section from the projected geometry described in section 5.5. Let $f(x, y)$ be the function describing the optical density distribution of the ring.

$$\tau_i = \int_{L_i} f(x, y) dl \quad (15)$$

In theory the ring has a continuous density distribution and therefore f is a continuous function. However it is necessary to be able to represent arbitrary functions easily. The digital representation used for f is a set of discrete and regularly spaced sample points, in the same way that images are represented with pixels. Let f_j , $j \in [1, N]$ be the values of those samples. The discretization takes the form:

$$f(x, y) = \sum_j f_j h_j(x, y)$$

Where $h_j(x, y)$ is called an interpolation kernel. This kernel is such that $h_j(x, y) = 1$ when (x, y) is the location of sample point j , so that the value of f is unchanged

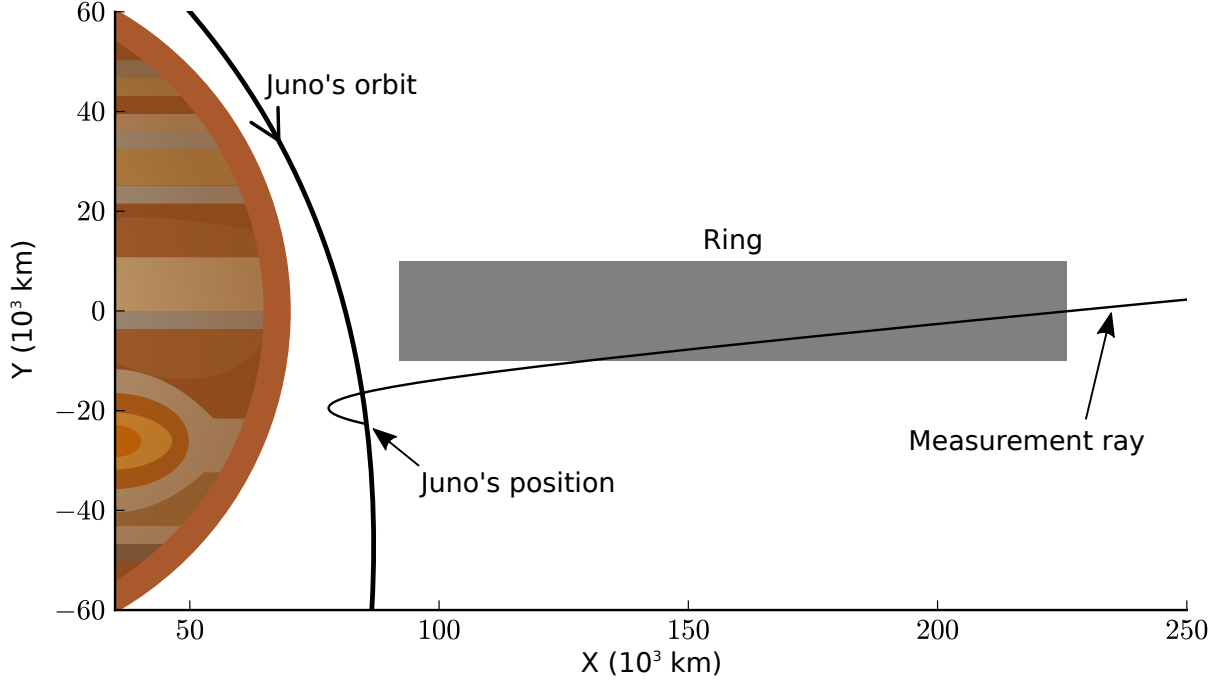


Figure 16 – Example of one measurement ray in the projected (ρ, Z) plane and estimated position of the ring. This configuration is from science orbit 1, on 2016-10-30 at 17:55:32 UTC, CHU A at RA -157.0° , DE 5.2° .

there. Outside of sample points, one can use linear interpolation to reconstruct a value for f . A description of the kernel used here is below where (x_0, y_0) is the position of sample j .

$$h_j(x, y) = g(x - x_0, y - y_0)$$

$$g(x, y) = \begin{cases} 1 - |x| - |y| + |xy| & \text{if } |x| < 1 \text{ and } |y| < 1 \\ 0 & \text{otherwise} \end{cases}$$

Equation (15) becomes:

$$\tau_i = \int_{L_i} \sum_j f_j h_j(x, y) dl$$

$$\Leftrightarrow \tau_i = \sum_j \int_{L_i} h_j(x, y) dl f_j$$

Let G be a matrix of size $M \times N$ such that:

$$G_{ij} = \int_{L_i} h_j(x, y) dl \quad (16)$$

The problem of reconstructing the ring's structure is then a linear inverse problem:

$$\tau_i = \sum_j G_{ij} f_j \Leftrightarrow \mathbf{d} = \mathbf{Gf} \quad (17)$$

Where \mathbf{d} is the vector of observations, \mathbf{f} is the unknown model vector representing the optical density profile, and \mathbf{G} is the model matrix of size $M \times N$ with M the number of measurements, and N the number of sample points (pixels).

Calculating the G matrix from equation (16) is a numerical integration problem sometime known as *forward projection*. One can simply use the midpoint method with a step-size parameter Δ_l , chosen smaller than half the pixel size to avoid aliasing.

$$G_{ij} = \sum_{x,y \in L_i} h_j(x,y) \Delta_l$$

Solving equation (17) for \mathbf{f} yields the internal structure of the ring, in the form of the optical depth distribution as a function of (x, y) , where x is the radial distance to Jupiter's rotation axis and y is the coordinate along Jupiter's rotation axis.

The number of sample points N determines the model resolution. Together with the rank of \mathbf{G} , it is critical to the form of the inverse problem defined by equation (17). Nevertheless, the image reconstruction problem will typically be under-determined because of the constraints on the observation geometry and number of imaging opportunities. Methods exist to address under-determined tomographic problems as described in section 4.7. Some allow to incorporate priors to the reconstructed distribution which helps to relate the current knowledge of the physical structure. There are for example iterative methods, maximum entropy methods (MEM) [16] or maximum likelihood methods (ML), although these will not be described in this report.

6 Model and Validation

This chapter presents the experimental work performed to validate the method of the analysis proposed. The experimental model contains two parts. First, an experimental setup is used to produce artificial data with an engineering model of the Advanced Stellar Compass. Then, this data is fed to a proof-of-concept software intended to demonstrate the feasibility of the tomographic reconstruction of the structure of the Jovian rings.

6.1 Experimental setup

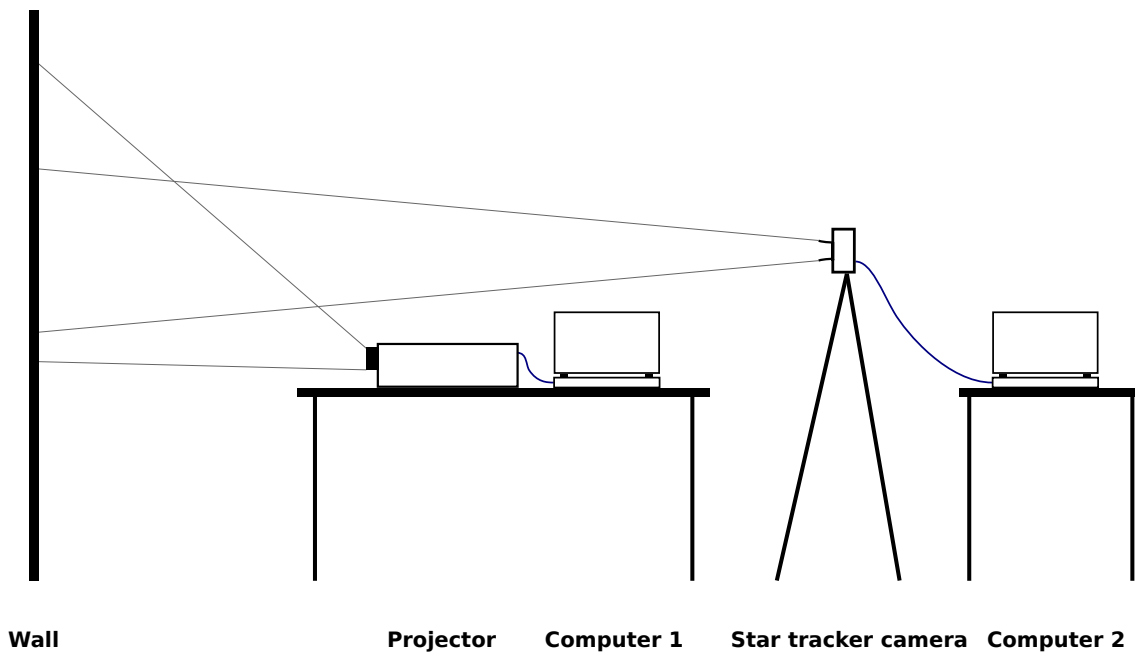


Figure 17 – Schematic representation of the experimental setup.
Distances and angles are not to scale.

The purpose of the experimental setup is to obtain artificial and realistic images simulating the data that will be obtained by the Juno spacecraft when it orbits Jupiter. Figure 17 shows the configuration of the setup used. The Advanced Stellar Compass used is identical to the flight-unit on Juno. It is pointed horizontally at a wall illuminated by a standard video projector. The projector and camera are controlled by two different computers for practical reasons. The distance between the camera and the wall is approximately 6 meters, such that its 13° field of view fits inside the area illuminated by the projector. Increasing the distance of both the projector and the camera to the wall improves the sharpness of stars on the wall, but there are limitations due to the size of the wall and the laboratory room.

Software used for controlling the star camera was provided. It allows setting the exposure time, commanding image capture and downloading raw data (bmp format) to the computer. However, custom software described in this chapter is used for rendering stars, called the planetarium.

The planetarium software renders stars with accurate positions and relative magnitudes, using radiometric calibration data of the projector. Methods for dealing with the large range of magnitudes and the pointing attitude are described in sections 6.3 and 6.4.

Optical attenuation due to the ring passing between the star and the camera is also simulated (6.5), together with the projected orbit of Juno obtained from JPL's science data (6.6).

6.2 Radiometric calibration

Let $\Gamma(p)$ be the function that associates to a pixel value the total intensity measured at the acquired image. It includes the effects of the internals of the projector, reflectance of the wall, distance of the camera to the wall, aperture size, detector area, shutter time and quantum efficiency.

In order to simulate accurate relative star magnitudes a good model of Γ is needed. This is the purpose of calibration. By following the steps described in section 5.3 a calibration procedure has been followed:

1. Threshold to remove background noise
2. Extract star region of interest using connected components
3. Use weighted mean to find the center of mass
4. Integrate to find intensity

The calibration image has been produced with the setup shown in figure 17 and the procedure above mentioned has been applied.

Thresholding

A histogram of one of the images taken can be seen here for a shuttertime of 10ms:

From this the noise level was determined to be 0.2 (pixel value 51), which has then been used as the thresholding value t . When the thresholding is performed with this value, the following transformation can be seen on figure 19 (zoomed in on 4 pixels in down right corner, 10ms shutter time).

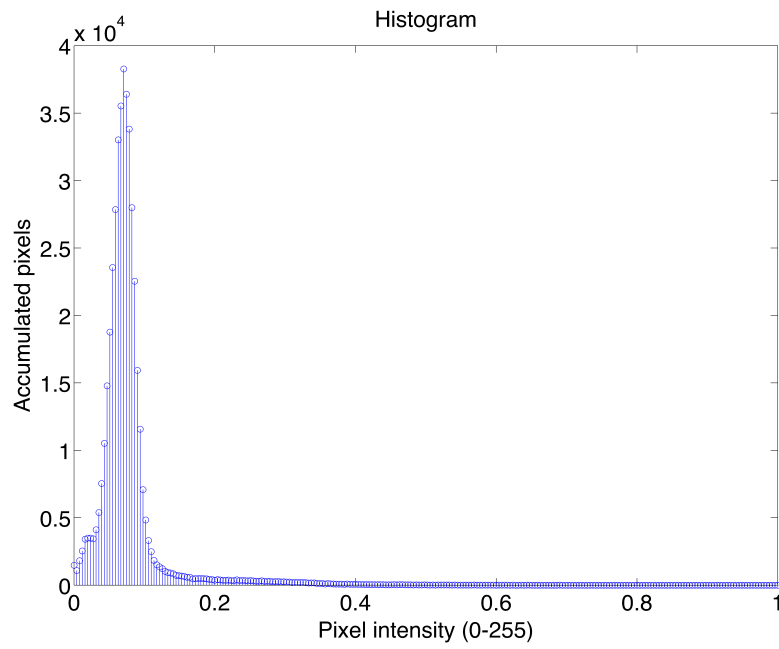


Figure 18 – Histogram of image with 10 ms shutter time



Figure 19 – Effects of thresholding with 0,2 relative value for calibration image with 10ms shutter time. Down right corner of image. Left is before thresholding and right is after thresholding.

As seen on figure 19, the extend of the star is largely cut down on this example and a lower thresholding could possible have been chosen, but in order to sustain a comparable output from different shutter times the value of 0.2 has been chosen for all images, as this fits better with other images of different shuttertimes.

Intensity

As the star region of interest and weighted mean center is not interesting in this case, the last step of intensity measurements is described here. By integrating the intensities as described in section 5.3 and correlating this with the outputted intensity from 0 to 255 to the projector for 3 different shutter times, the following has been produced:

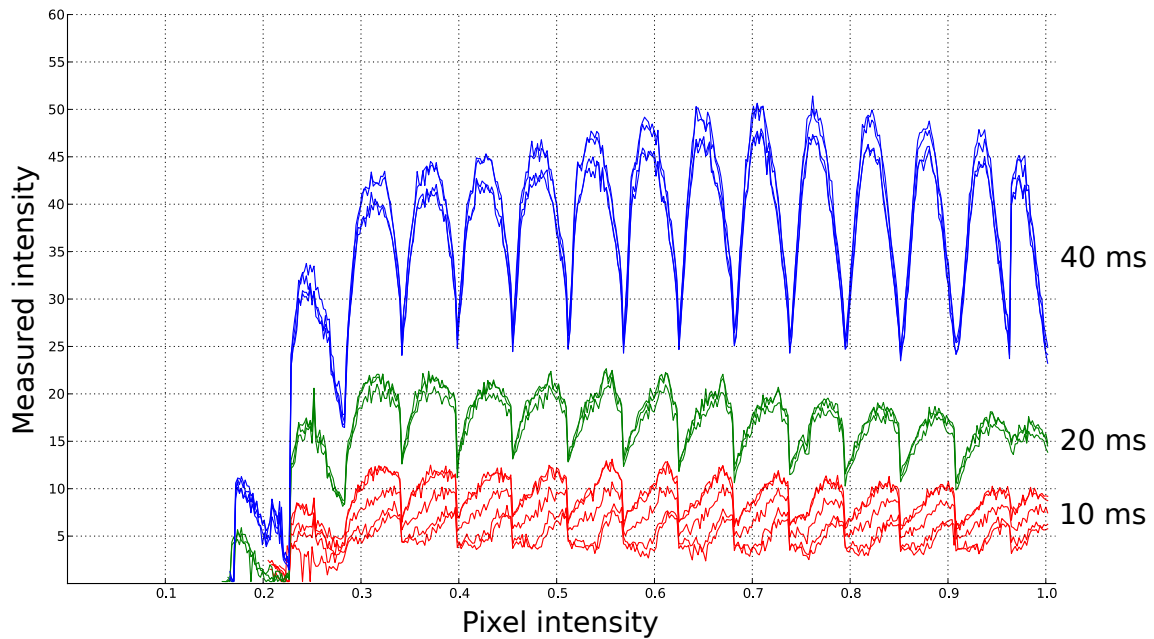


Figure 20 – Result of calibration images with shuttertimes of 10, 20 and 40 ms.

As it can be seen in figure 20 the intensities rise as the shutter time increases as expected, and also with an expected correlation with the amount of shuttertime (40ms shuttertime is about double intensity as the 20ms shuttertime).

Unfortunately it can also be seen that there is very little correlation between the outputted intensity and measured intensity. There is an oscillation in measured intensities from the calibration image which is likely to come from one or more of the error sources described below. One of the images that were obtained from the calibration is showed in figure 21.

As it can be seen in figure 21, the radial distortion is very apparent when observing "stars" that are off-center of the image. This radial distortion is mainly due to the fact that the image plane is not a sphere. Further more the image is observed as out of focus, due to the camera being set for focus to infinity.

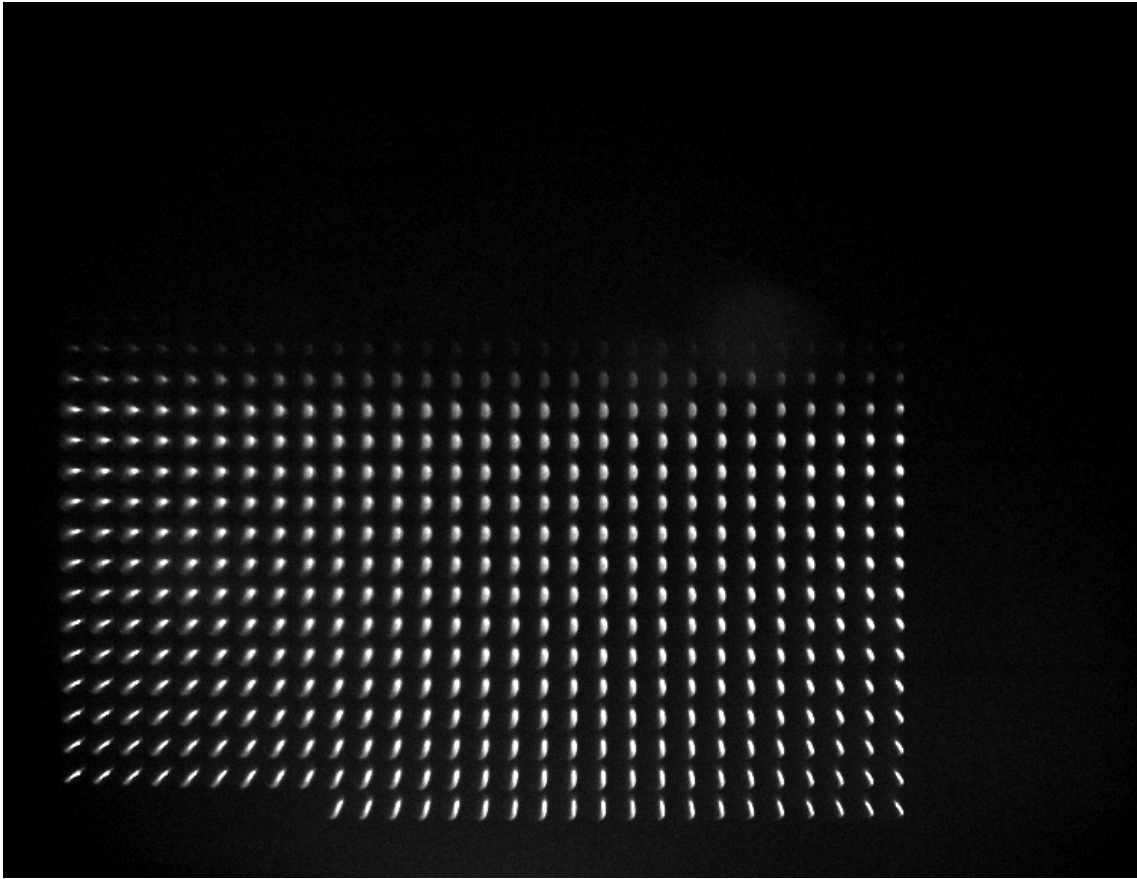


Figure 21 – Calibration image taken from star camera with 40ms shuttertime. The radial distortion is very apparent.

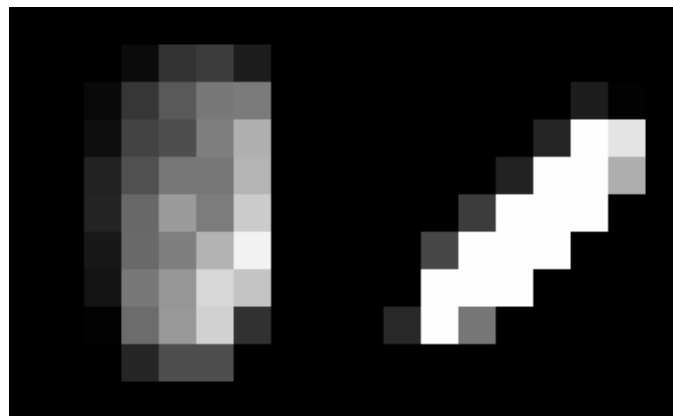


Figure 22 – Two examples of the camera's point spread function. On the left, the response to a low intensity pixel with little radial distortion and a high intensity pixel with high distortion on the right.

The radial distortion does not seem to origin from the projector itself, as there has been taken measures to ensure a distortionless projection of the images from the projector.

When correlating the calibration images with the intensity-plot in figure 20, it is apparent that the oscillations are in connection with the number of rows in the image. The intensity is directly connected to the sideways position on the image, and the intensity increases as the position gets closer to the middle of the image. The following noise sources have been found and investigated:

Radiance variations from different angles

Due to the fact that the radiance varies with angle off the surface that it emits from, this is a possible source of error. When holding this together with the oscillations and intensity variations, it seems that this is a very likely explanation to the varying intensity measurements.

Spread of pixel values due to radial distortion

As mentioned before, a very apparent distortion in the image is the radial distortion. As zoomed in on in figure 22, the radial distortion greatly shifts the extend of the observed "star" as well as moves the spread of pixel values. As an example two histograms are shown below. Both are taken from a calibration image, and the histograms shown are accumulated over 10 stars in both highly distorted area and low distorted area.

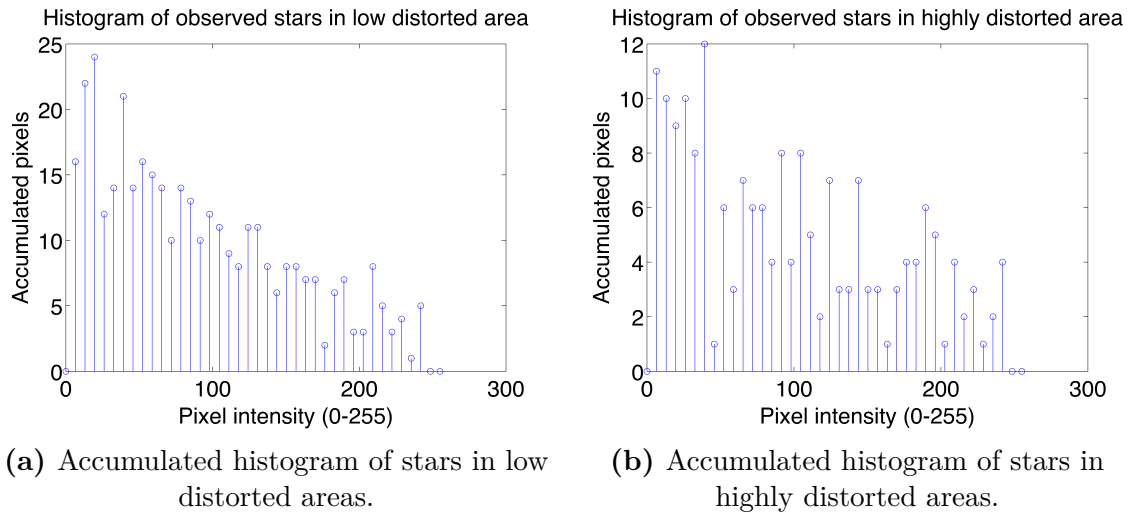


Figure 23 – Accumulated histograms of stars in highly and low distorted areas. All are made with 40 bins to compensate for low number of pixels. All histograms are from pixel value 2 to 250, due to the black background and high number of saturated pixels.

The histograms above are accumulated histograms each existing of 10 images of stars, one in highly distorted area and the other in low distorted area. Both histograms are made with 40 bins in order to compensate for low number of pixels in

the star images. Further more both the histograms are shown without value 0-2 and 250-255. This is done because they distort the histograms, as there are a large number of black background pixels, and also a large number of saturated pixels.

It can be seen that the observed intensities in the low distortion are concentrated in the low intensity area, i.e. confined to the lower values. There are also a greater amount of low intensity pixels compared to the highly distorted area. It is visible that the highly distorted area stars have a more equal spread of intensities, which is most likely due to the fact that the outputted intensity from the projector is smeared along a radial distortion.

All in all this difference in spread may have led to a difference in summed intensity, both due to the thresholding filtering that is applied and due to the number of saturated pixels in the image taken. As an example in an image taken with 20 ms shuttertime, the number of saturated pixels in highly distorted area, summed over 10 images, was 44 compared to a low distortion area with 108 saturated pixels.

Noise from projector

When viewing the images taken for optical depth sensitivity it becomes very apparent that a large noise factor is the projector "black" areas. These are areas in the image that are suppose to be black, but are being lid up by the projector. This is very visible in figure 24 where the noise from the projector can clearly be seen.

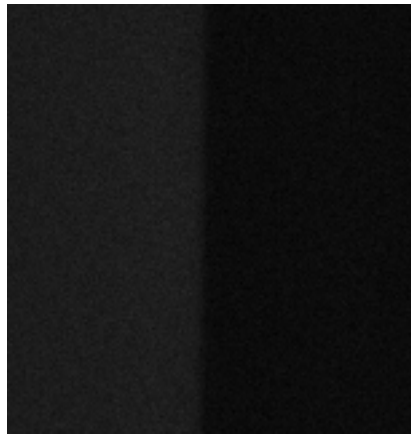


Figure 24 – Cut-out of area in the image where projector-noise is very apparent. At the left is an outputted "black" area from the projector, and on the right is the wall being projected on. Image taken with 5ms shuttertime.

As seen on figure 24, the projector adds a lot of noise in the areas where it supposed to be black.

The noise in the dark areas is no threat to the image analysis, as these lay beneath the noise filtering level, which can be seen in figure 19, but the noise might add to the total intensities of stars.

Dusty lenses in projector

It was found that the projector had some dust in the lens system. This was unfortunately found after images were taken, and could therefore not be taken into account before the images were acquired. It does not seem that this has a great effect on the measured intensities, as the dust particles seems to affect areas outside the star rendering. It is estimated that this is not a major contributor to noise in the images.

6.3 Star rendering

Apparent stellar magnitude is relative and obeys:

$$m - m_{ref} = -2.5 \log_{10} \left(\frac{I}{I_{ref}} \right)$$

Here I is the intensity in $\frac{W}{m^2}$ and m is the unit-less apparent magnitude. Then, displaying a star with intensity I is simply a matter of finding p such that:

$$\Gamma(p) = I = I_{ref} 10^{\frac{m_{ref} - m}{2.5}} \quad (18)$$

Having established a numerical model for Γ^{-1} with the process of calibration, this would be straightforward. However there are two problems with this simple approach. First, only one pixel is used to represent a star which does not look realistic to the eye. In all representation of stars, including the one made by the human retina, stars look like small circles because of the point spread function of the imaging system. Secondly, the intensity range of a pixel, $[\Gamma(0), \Gamma(1)]$ is quite limited and very noisy.

But equation (18) shows that star intensities are expected to cover many order of magnitudes. To address those two issues, an artificial point spread function is used. Instead of rendering a star as one single pixel, a gaussian function is convoluted with the pixel grid:

$$G_{\alpha, \sigma}(x, y) = \alpha \exp \left(-\frac{x^2 + y^2}{\sigma^2} \right)$$

Where α and σ^2 are two parameters: amplitude and spread. The total intensity emitted by the star is now:

$$\int_{-\infty}^{\infty} \int_{-\infty}^{\infty} G_{\alpha, \sigma}(x, y) dx dy = \alpha \sigma^2 \pi$$

This lets us adjust α and σ independently to achieve a greater intensity range. Equation (18) becomes:

$$\begin{aligned} I &= \alpha \sigma^2 \pi \\ \Gamma(p) &= G_{\alpha, \sigma}(x, y) \end{aligned} \quad (19)$$

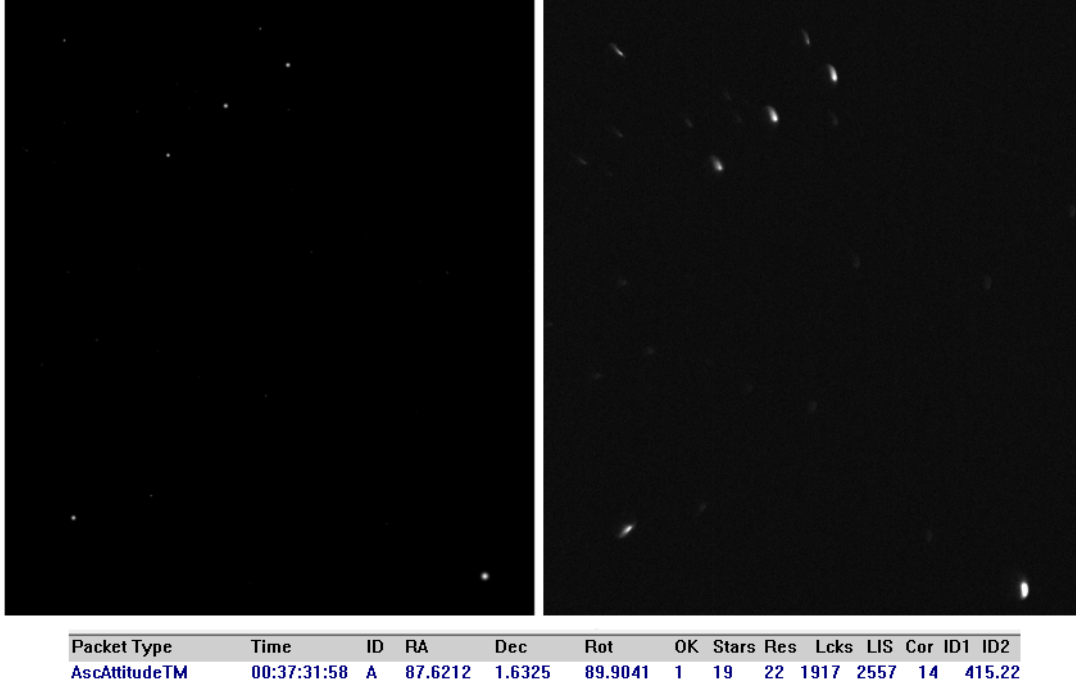


Figure 25 – Orion constellation rendered on the projector (left) and image acquired by the star camera (right). The attitude shown is 86° by 2° . The reported attitude (bottom) is 87.6° by 1.6° .

The maximum intensity value of a pixel is I_{ref} , therefore with a fixed spread σ_0 , the maximum achievable intensity is $I = I_{ref}\sigma_0^2\pi$. α and σ are chosen in the following fashion.

$$\text{If } I \leq I_{ref}\sigma_0^2\pi, \begin{cases} \alpha = \frac{I}{\sigma_0^2\pi} \\ \sigma = \sigma_0 \end{cases} \quad \text{If } I > I_{ref}\sigma_0^2\pi, \begin{cases} \alpha = I_{ref} \\ \sigma = \sqrt{\frac{I}{I_{ref}\pi}} \end{cases}$$

In the experimental setup, a reference star is chosen with a magnitude m_{ref} given by the star catalogue and reference intensity of $I_{ref} = \Gamma(1)$. This way, changing the reference star shifts the whole intensity range up or down in intensity but preserves the correct relative star magnitudes.

6.4 Planetarium using the Hipparcos catalog

Using the Hipparcos catalogue (see section 4.5), stars are drawn at the position at which the camera would see it if it was in space, observing the celestial sphere. The geometric parameters of the setup were measured with a laser range finder. Let the camera-wall distance be d and the offset between the camera optical center and the center of the wall area be (w, h) . Knowing the right ascension RA and the

declination DE of a star, finding its (x, y) coordinate on the wall is a simple matter of trigonometry:

$$\begin{aligned} x &= w + d \tan RA \\ y &= h + d \tan DE \end{aligned} \tag{20}$$

The final step is to convert this result to pixel coordinates using the ratio of resolution to screen size. Arbitrary pointing attitude is handled by translating stars' coordinates modulo 2π . At this point, the stellar compass is able to reconstruct its virtual attitude to within about 1° as shown by Figure 25, where the left image is the produced image and the right image being the image observed by the star camera. Below is an outputted attitude of the star camera software showing a lock on attitude.

6.5 Optical depth

This section validates the part of the analysis that estimates the optical depth from intensity measurements as described (section 5.3.2). Previously was described a method for rendering a star with a given intensity I . Following this, it is also possible to simulate a specific optical depth by applying the well known relation:

$$I = I_0 \exp(-\tau)$$

This was performed in the experimental setup with τ ranging from 10^{-4} to $10^{-0.5}$ in logarithmic space. Because of optical radial distortion and random noise sources, intensity is highly dependent on location in the projected image. To mitigate this, the reference star of each calculation is positioned just above the attenuated one, as shown in figure 26. Then, optical depth is calculated from the acquired image using the procedure described earlier in the analysis (sections 5.3 to 5.3.2).

Figures 27, 28 and 29 show the results of the estimation procedure averaged over six acquisitions for three different intensities and exposure times. The errorbars indicate standard deviation and τ_{min} is the value estimated from the graph after which the signal is strong enough to be detected.

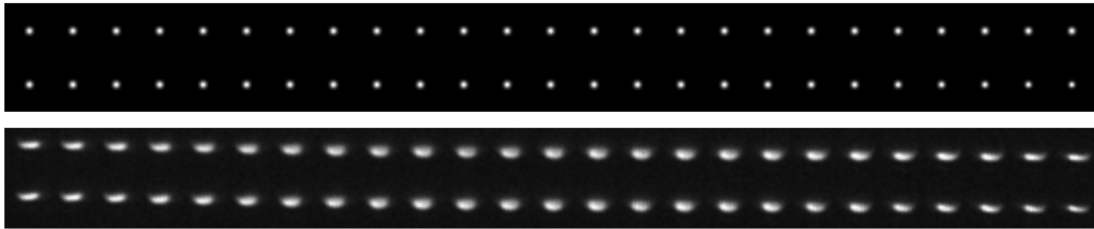


Figure 26 – Image used for simulating intensity attenuation, here with $I = 25$ and $\delta t = 1$ ms. The upper image was displayed on the projector and the bottom image was acquired by the camera. Attenuation is from left to right ($\tau = 10^{-4}$ to $10^{-0.5}$).

As expected, the faintest optical depth is detected using the strongest intensity (figure 29). It corresponds to an attenuation of about 3.5%. Below this, the noise dominates and the optical depth is not reliable. Importantly, this limit is not the limit of the star camera, but it is caused by the limitations of the experimental setup and associated noise. If anything, it shows the existence of the τ_{min} limit and its manifestation as the attenuation of light changes.

Estimating the achievable τ_{min} of the star camera experimentally would require laboratory equipment more accurate in intensities than a simple video projector. Without it, the best one can do is carefully consider the terms of equation (12).

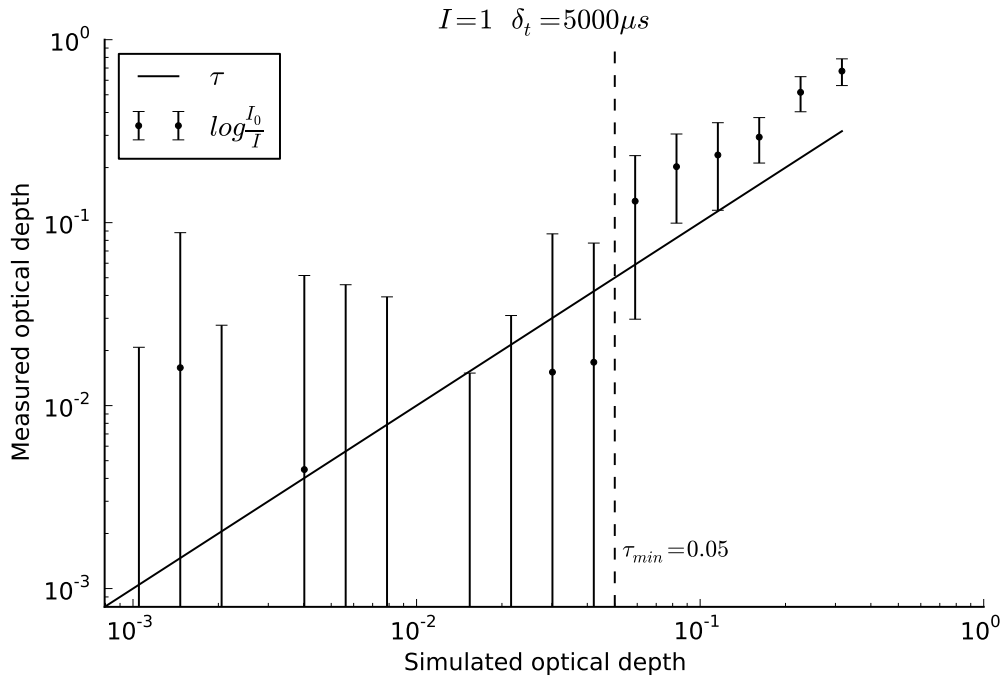


Figure 27 – Estimation of optical depth τ from simulated starlight attenuation with low intensity and shutter time.

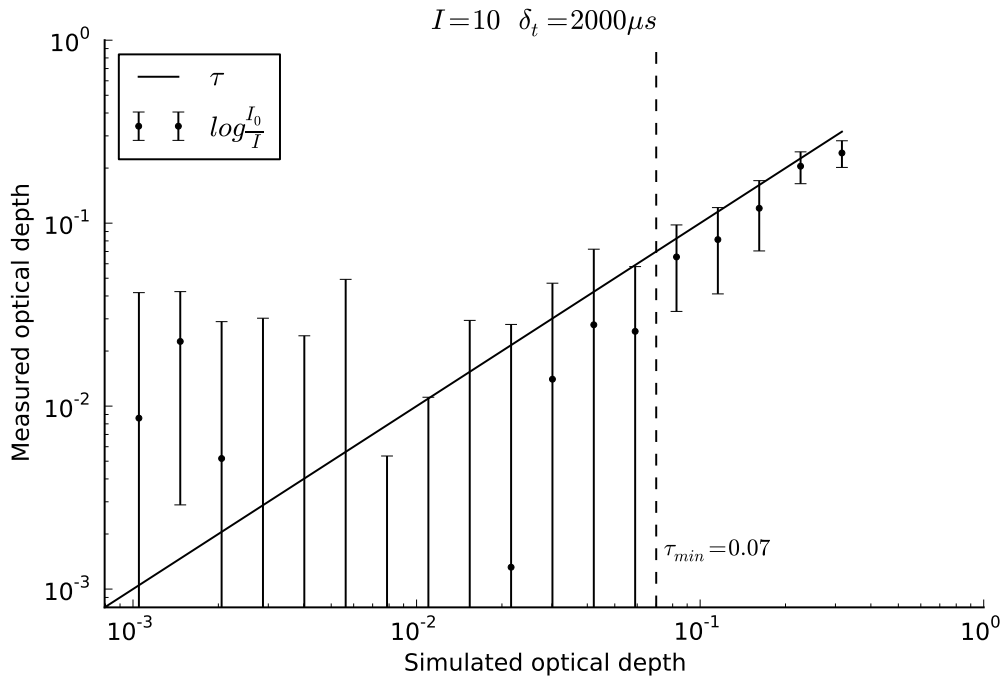


Figure 28 – Estimation of optical depth τ from simulated starlight attenuation with medium intensity and shutter time.

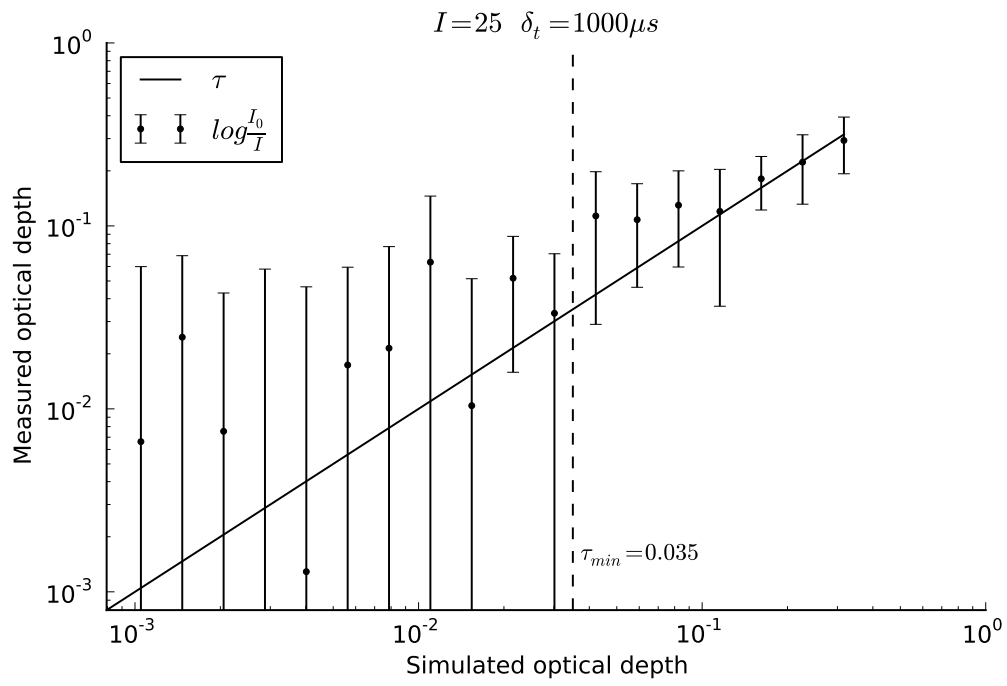


Figure 29 – Estimation of optical depth τ from simulated starlight attenuation with high intensity and shutter time.

6.6 Juno orbit simulation with SPICE

The Navigation and Ancillary Information Facility (NAIF), releases the SPICE toolkit. SPICE is "an observation geometry system for planetary science missions" [1]. It is a very powerful software toolkit, allowing the user to query complex operation and science parameters.

In the context of this project it is extremely useful for selecting observation opportunities. Data is available describing the orbits of Juno and its attitude with high precision. Conveniently, SPICE can output data in any reference frame, allowing to work directly in Jupiter centered coordinates. It was used to produce the data needed for figure 16.

6.7 Software

This section briefly described the software that was written for this project.

Radiometric calibration

The OpenCV [`opencv`library`] and C++ were used for producing the radiometric calibration images displayed on the projector. The software produces an image with single pixels of increasing intensity, from dark to fully bright.

Planetarium

The planetarium described in sections 6.3 and 6.4 also uses OpenCV and C++.

Optical depth simulation

To simulate optical depth (section 6.5) and produce the images like the one shown in figure 26 OpenCV and C++ were also used.

SPICE

To extract Juno state vector and instrument attitude information in Jupiter centered coordinates required the use of the CSPICE library. It is the toolkit provided by NAIF for reading and querying the Juno kernel data files.

Post processing and plotting

Python and the matplotlib [7] library were extremely useful for processing calibration and optical depth data, as well as produce many figures in this report.

7 Conclusion

This report investigated the exciting possibility of studying the interior of the poorly understood rings of Jupiter. The occultation profiling technique was described and applied to the problem of reconstructing interior optical depth.

Through a study of existing literature about the Jovian rings, an introduction to the relevant theory of light attenuation and tomography was exposed. Then, analysis described in details the steps required to process star camera images into a vertical cross section of the ring.

Finally, critical parts of the methods were investigated with experimental work. An engineering model of the instrument on board Juno produced artificial image data in the laboratory, which was used for testing. Together with trajectory information from NASA's mission planners, custom written image analysis software completed the analysis of this unique science opportunity.

The possibility of profiling Jupiter's rings with the Juno spacecraft is real, but not without challenges. The spacecraft attitude is well-known due to the mission's primary objective. This allows long exposure times, which increase the sensitivity of the system to a faint optical depth. Even though smearing was not investigated, the effects of rotation during image capture can be dealt with by careful modelling or correction during preliminary image processing.

A more practical challenge is the development of the tools without the required data. Simulating artificial stars is very helpful, but one is rapidly faced with the limitations of terrestrial equipment in producing light sources as precise as star which spanning up to seven or eight orders of magnitude.

The test setup used in this project did not have the sufficient invariance or sensitivity to completely demonstrate the feasibility of the method. However, it had a high enough precision for attitude determination using the star camera, and for representing the stars which Juno will experience when orbiting Jupiter.

Hopefully this project is the beginning of the serious consideration of this additional scientific possibility that Juno offers.

8 Future work

This project was limited by time and resources, therefore a lot of interesting work remains to be done if a perfect result is to be obtained.

Only attenuation of light was studied here. Forward scattering is another physical process present in the rings as explained in section 3.2. A careful consideration of Mie scattering is an equally good possibility for studying the rings with the Juno mission.

In the analysis, the next important step is taking into account the motion smear caused by the continuous rotation of the spacecraft. Two possibilities exist. The first one is to apply a de-smearing algorithm, which will simply reverse the effect of that distortion. However, this limit the exposure time to the time needed for one full rotation of the spacecraft. The other possibility is to work directly with the smeared image, and take into account the rotation in the data processing. It is expected that this latter method will lead to better results.

A further assumption about the structure of the rings could be made, leading to even greater density of observations with the same data. Perhaps the rings are vertically symmetric. In other words, the equator is a plane of symmetry, and optical depth is similar on either sides. This leads to half the model parameters for the same data, which means that the achievable resolution could potentially be doubled, as depicted in figure 30.

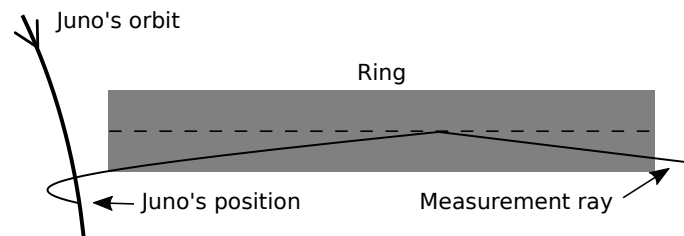


Figure 30 – What a measurement ray through the ring could look like with an additional assumption of vertical symmetry. Observation density is doubled.

Some geometry considerations were skipped over in this work. The SPICE software toolkit returns orientation data in Earth's equatorial coordinates. There is a non negligible offset between Jupiter's equatorial plane and Earth's equatorial plane. Therefore, software used for the actual tomographic reconstruction of the rings will need to take this into account.

The motion of Juno together with the Jupiter system and its moons is complex. Imaging opportunities have to carefully consider the presence of moons in the image, the presence of Juno and Jupiter and light reflected off Jupiter's clouds and which parts of the ring are occulted. This could be addressed either manually if the

number of images if low enough, or automatically with the development of a moon elimination filter for example.

Another important study to be made is an accuracy analysis of the system. Taking into consideration visible stars, spacecraft position and all the problem's geometry, what resolution is achievable? Which exposure time is necessary, and how does that compare with the operational possibilities of the spacecraft?

An excellent decision tool would be to find optimal viewing geometry and image acquisition parameters for each number of images acquired, possibly using the Celestia program. For example, given that mission planners allow five images to be downlinked to Earth, what are the optimal parameters? What if they allow ten images? And for each of those options, what is the expected resolution of the tomographic image reconstruction? This would be valuable information for deciding if this experiment is to be performed when Juno reaches Jupiter in 2016.

References

- [1] Acton, C.H.; "Ancillary Data Services of NASA's Navigation and Ancillary Information Facility," *Planetary and Space Science*, Vol. 44, No. 1, pp. 65-70, 1996. URL: <http://naif.jpl.nasa.gov/naif/toolkit.html>.
- [2] Joseph A Burns, Douglas P Hamilton, and Mark R Showalter. "Dusty rings and circumplanetary dust: Observations and simple physics". In: *Interplanetary Dust*. Springer, 2001, pp. 641–725.
- [3] *Discrete tomography*. URL: https://en.wikipedia.org/wiki/Discrete_tomography.
- [4] Larry W Esposito. "Planetary rings". In: *Institute of Physics Publishing, LASP, University of Colorado* (2002).
- [5] Pierre Grangeat and Wiley InterScience (Online service). *Tomography*. Translation of: La tomographie and La tomographie medicale, originally published by Hermes Science/Lavoisier, 2002. London; Hoboken, NJ: ISTE ; John Wiley, 2009. ISBN: 9780470611784 0470611782 9780470610374 0470610379. URL: <http://site.ebrary.com/id/10361132> (visited on 10/27/2014).
- [6] Berthold Klaus Paul Horn. *Robot Vision*. The Massachussets Institute of Technology, 1986.
- [7] J. D. Hunter. "Matplotlib: A 2D graphics environment". In: *Computing In Science & Engineering* 9.3 (2007), pp. 90–95.
- [8] *Interstellar dust, lecture notes Ohia State University*. URL: <http://www.astronomy.ohio-state.edu/~pogge/Ast871/Notes/Dust.pdf>.
- [9] *JUNO space mission*. URL: http://www.nasa.gov/mission_pages/juno/overview/index.html#.VEoP0EuPaKs.
- [10] Steve Matousek. "The Juno New Frontiers mission". English. In: *ACTA ASTRONAUTICA* 61.10 (2007), pp. 932–939. ISSN: 00945765, 18792030. DOI: 10.1016/j.actaastro.2006.12.013.
- [11] Maureen E Ockert-Bell et al. "The structure of Jupiter's ring system as revealed by the Galileo imaging experiment". In: *Icarus* 138.2 (1999), pp. 188–213.
- [12] Tobias Owen et al. "Jupiter's rings". In: *Nature* 281 (1979), pp. 442–446.
- [13] MAC Perryman et al. "The HIPPARCOS catalogue". In: *Astronomy and Astrophysics* 323 (1997), pp. L49–L52.
- [14] from Wikipedia Princeton University. URL: http://www.princeton.edu/~achaney/tmve/wiki100k/docs/Optical_density.html.
- [15] *Radon transform*. URL: https://en.wikipedia.org/wiki/Radon_transform.
- [16] John Skilling and RK Bryan. "Maximum entropy image reconstruction: general algorithm". In: *Monthly Notices of the Royal Astronomical Society* 211.1 (1984), pp. 111–124.

- [17] HB Throop et al. “The jovian rings: new results derived from Cassini, Galileo, Voyager, and Earth-based observations”. English. In: *ICARUS* 172.1 (2004). Ed. by Candice J. Hansen Phil Nicholson Dennis L. Matson, pp. 59–77. ISSN: 00191035, 10902643. DOI: 10.1016/j.icarus.2003.12.020.